ARTICLES
https://doi.org/10.1038/s41566-020-0690-1

nature photonics

Vectorized optoelectronic control and metrology in a semiconductor

Shawn Sederberg[1,2]✉, Fanqi Kong[1], Felix Hufnagel[3], Chunmei Zhang[1], Ebrahim Karimi[2,3] and Paul B. Corkum[1,2]

The increasingly prominent role of light in information processing makes optoelectronic devices a technology of fundamental importance. Coherent control of currents in semiconductors using synthesized optical waveforms provides a sensitive and robust means to transfer information from light to an electronic circuit. Currents driven by Gaussian laser beams are spatially uniform in direction, offering limited technological utility. Full control over the transverse spatial distribution of currents excited in a material would vastly increase the versatility and impact of optoelectronic devices. Here we simultaneously control the waveform and vectorial arrangement of optical fields, enabling precise manipulation of the spatial distribution of currents in a semiconductor. As a direct application, we drive loop currents, embodying a new ultrafast magnetic field source. Subsequently, we demonstrate a scheme for generating an arbitrary superposition of two orthogonal current arrangements via subcycle adjustment of the optical waveform.

Exploiting the waveform of light rather than solely its intensity has enabled revolutionary control over light–matter interaction[1]. Coherent control emerged as a technique in physical chemistry whereby an optimized optical waveform was used to steer a quantum system into a particular final state. In general, subtle modifications to the waveform adjust quantum interference in the interaction, substantially influencing its outcome. Since its inception, coherent control has matured into a powerful tool in areas as diverse as quantum optics and metrology[2–4], attosecond metrology[5,6], optoelectronics[7] and laser cooling[8,9].

Here we consider electronic transitions from the valence band into the conduction band of a semiconductor that are excited simultaneously through parallel quantum pathways, that is, two-photon absorption using light with angular frequency, ω, and linear absorption using its second harmonic, 2ω. Interference between two quantum pathways enables control over the resulting momentum distribution in the conduction band, depicted schematically in Fig. 1a, changing the amplitude and direction of currents in the semiconductor (Supplementary Note 1). In particular, currents can be controlled by adjustment of the relative phase between the two fields, $\Delta\varphi_{\omega,2\omega}$. These currents are typically detected directly using a pair of integrated electrodes, or indirectly by measuring terahertz pulses radiated from the transient current.

Current control using linearly polarized Gaussian laser beams has been demonstrated in quantum wells[10,11], semiconductors[12–17], dielectrics[18,19], metals[20], carbon nanostructures[21], nanoplasmonic structures[22] and two-dimensional materials[23]. In each of these cases, the uniform electric field vector across the beams (Fig. 1b) produces a directionally uniform current in the sample (Fig. 1c).

More broadly, optical excitation can transfer the quantum properties of photons to electrons in a semiconductor. For example, circularly polarized light has been used to photoemit spin-polarized electrons from negative-electron-affinity gallium arsenide (GaAs)[24,25]. To a similar end, the circular photogalvanic effect can be observed when circularly polarized light is applied to systems exhibiting valence-band spin splitting. For a given photon energy and polarization state, optical selection rules determine the resulting momentum distribution, providing a route to spin-polarized photocurrents[26–28]. Applying circularly polarized $\omega/2\omega$ beams to coherent control in semiconductors or quantum wells enables 'sorting' of electron spins in momentum space, producing pure electron 'spin currents' without an accompanying charge current[29–32].

Vector beams and vortex beams have enabled substantial advances in quantum communications[33,34], telecommunications[35], microscopy[36] and optical tweezers[37]. Photons comprising vortex beams carry two quanta of angular momentum: one from their spin and the other from the orbital angular momentum (OAM) carried on their spatial structure. Using trapped ions excited by vortex beams, it has been demonstrated that both quanta of angular momentum are transferred during an electronic transition, establishing new selection rules[38]. Simulations suggest that when terahertz vector or vortex beams are applied to semiconductor nanorings, the vector structure and OAM of the beam are imparted to charge oscillations and currents in the nanoring[39,40].

Results

Coherent control with vector beams. It is therefore also intriguing to apply vector and vortex beams to coherent control processes. Doing so would provide the possibility to uniquely define the momentum vector imparted to electrons excited by each coordinate of the beam. Such control would enable dynamic manipulation of complex current patterns, $|i\rangle$, with a spatial resolution approaching the diffraction limit, establishing a new era in optoelectronics.

We first consider an azimuthal vector beam, with the electric field mode shown in Fig. 1d. When two azimuthal beams at ω and 2ω excite a semiconductor, the current vector will be aligned along the local electric field. Electrons will be given momentum in the azimuthal direction, and the resulting current vector distribution will resemble current flowing around a loop, as illustrated in

[1]Joint Attosecond Science Laboratory, University of Ottawa, National Research Council Canada, Ottawa, Ontario, Canada. [2]Max Planck - uOttawa Center for Extreme and Quantum Photonics, Ottawa, Ontario, Canada. [3]Department of Physics, University of Ottawa, Ottawa, Ontario, Canada.
✉e-mail: shawn.sederberg@uottawa.ca

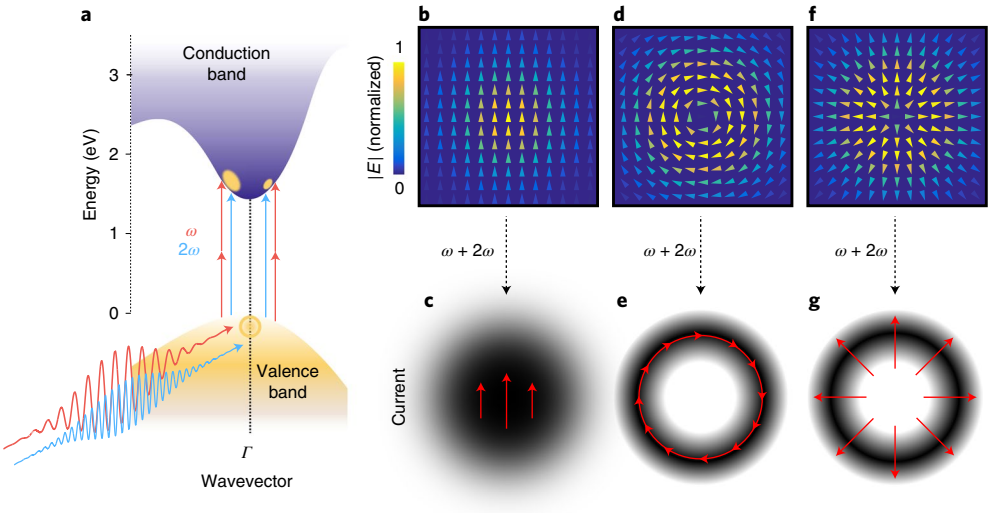

Fig. 1 | Vectorized coherent control. a, Electronic band structure of GaAs. An optical field at angular frequency 2ω can excite direct transitions to the conduction band, while another field at ω can excite two-photon transitions. The relative phase between the two light waves enables control over asymmetry in the momentum distribution of the conduction band population, driving current through the semiconductor. **b**, The electric field distribution of a Gaussian laser beam with linear polarization. **c**, Schematic depiction of the directionally uniform current produced when two Gaussian laser beams (ω and 2ω) are applied to a semiconductor. **d**, The electric field arrangement of a vector beam with azimuthal polarization. **e**, Illustration of the current resulting from azimuthal laser beams at ω and 2ω. **f**, The electric field configuration of a radially polarized vector beam. **g**, Sketch of radial currents produced by coherent control with two radial vector beams.

Fig. 1e. Similarly, radial vector beams at ω and 2ω (Fig. 1f) will produce radial currents (Fig. 1g).

We investigate these configurations using low-temperature gallium arsenide (LT-GaAs, bandgap energy $E_g = 1.5$ eV) as a semiconductor and the experimental setup shown in Fig. 2a (see Methods for further details). Femtosecond pulses at the fundamental wavelength, $\lambda_\omega = 1{,}482$ nm, are used to drive two-photon absorption, and pulses at the second-harmonic wavelength, $\lambda_{2\omega} = 741$ nm, are used to excite direct transitions. Each beam is independently converted into a vector mode using a liquid crystal plate, and an exemplary mode profile of an azimuthal beam is shown in Fig. 2b.

In contrast to conventional coherent control experiments, the non-uniform polarization of vector beams necessitates current sampling in subbeam-diameter pixels. To this end, an apertured LT-GaAs optoelectronic detector (depicted in the inset of Fig. 2a, further details in Supplementary Notes 2–4) is used to spatially resolve the local current vector in 28 μm × 25 μm pixels. We introduce azimuthally polarized beams to the detector and scan $\Delta\varphi_{\omega,2\omega}$ at two points situated in opposite halves of the mode, illustrated by points P_1 and P_2 in Fig. 2b. As shown in Fig. 2c, the two current traces oscillate out of phase because the local fields have opposite directions. This simultaneously demonstrates subfocal-spot current sampling and control over the amplitude and direction of currents in the semiconductor. Here the detected signal is proportional to the final momentum imparted to the conduction-band electrons, and does not contain details related to the intermediate polarization dynamics induced by the exciting fields.

Next, $\Delta\varphi_{\omega,2\omega}$ is adjusted to the peak current amplitude of the scan in Fig. 2c. Keeping $\Delta\varphi_{\omega,2\omega}$ constant, the detector is raster scanned across the beam profile in a Cartesian grid with 25 μm resolution in the x and y directions, that is $\Delta x = \Delta y = 25$ μm. Although this technique does not capture the complete current pattern at once, the substantially superwavelength (yet subbeam diameter) aperture dimensions ensure that the detected current provides an accurate pixel of the full bulk current, while being virtually free of convolution effects.

Due to the strong directionality of the current detector (Supplementary Note 5), the spatial orientation of the detector can be chosen such that it is predominantly sensitive to the x component of the current (I_x), shown in Fig. 3a. Rotating the detector by 90° and repeating the raster scan then isolates the y component of the current (I_y), presented in Fig. 3b. Combining I_x and I_y enables spatial mapping of the current vector (Supplementary Note 6), shown in Fig. 3c. The distinct loop current confirms that the azimuthal mode structure is transferred to the current.

Spatio-vectorial resolution of planar current elements enables us to calculate the resulting magnetic field via the Biot–Savart law:

$$\mathbf{B}(\mathbf{r}) = \frac{\mu_0}{4\pi}\int\int\int \frac{(\mathbf{J}\mathrm{d}V)\times\mathbf{r}'}{|\mathbf{r}'|^3}, \quad (1)$$

where μ_0 is the vacuum permeability, $\mathbf{J}$ is the current density, and $\mathbf{r}'$ is the displacement vector from a current density element to the point under evaluation. Applying this to the measured data produces the longitudinal magnetic field (B_z) distribution in Fig. 3d, which is valid in the plane of the detector. This magnetic field will be the basis for all-optical generation of terahertz magnetic field impulses in future work[41].

To demonstrate the generality of this concept, we consider the case where both beams have radial polarization. In a similar manner, we measure I_x and I_y across the beam, which are shown in Fig. 4a,b, respectively. The current vector mapping shows a ring-like shape, but the current is driven in the radial direction towards the beam centre, plotted in Fig. 4c.

Coherent control over the global current arrangement. The previous cases of radial and azimuthal current distributions can be thought of as orthogonal current modes, $|r\rangle$ and $|a\rangle$, respectively, and $\Delta\varphi_{\omega,2\omega}$ was used to control the amplitude and sign of a fixed mode. The ability to generate an adjustable superposition of orthogonal current modes via coherent control, that is $|i\rangle = c_r|r\rangle + c_a|a\rangle$, where c_r and c_a are the coefficients, would provide yet another degree of freedom for optoelectronic information processing.

Generation of orthogonal current arrangements requires full control over the local electron momentum in the transverse plane.

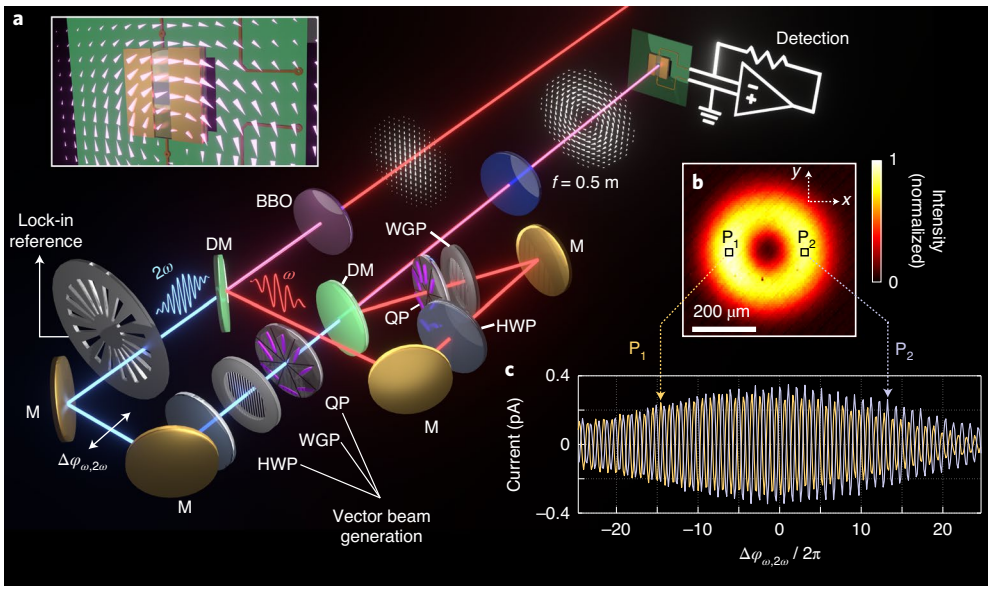

Fig. 2 | Experimental configuration. a, Schematic representation of the experimental configuration used to generate vector beams at ω and 2ω, and to synthesize their waveform. M, metallic mirror; DM, dichroic mirror; HWP, half-wave plate; WGP, wiregrid polarizer; QP, *q* plate; BBO, beta-barium borate crystal. An enlarged view of the apertured LT-GaAs detector is shown in the inset. **b**, Typical intensity profile of an azimuthal vector beam measured by a complementary metal–oxide–semiconductor beam profiler. The inset squares at points P_1 and P_2 depict the relative size of the LT-GaAs detector aperture. **c**, Detected *y* component of current as a function of $\Delta\varphi_{\omega,2\omega}$ measured at points P_1 and P_2 in the beam (shown in **b**). The out-of-phase oscillations confirm that the opposite electric field sign of the vector is transferred to the current and that this can be effectively sampled with the LT-GaAs detector.

Such control has previously been demonstrated in GaAs using two circularly polarized $\omega/2\omega$ Gaussian laser beams with the same handedness, where the current direction is determined by $\Delta\varphi_{\omega,2\omega}$: $\hat{\mathbf{m}} = \hat{\mathbf{x}}\sin(\Delta\varphi_{\omega,2\omega}) \pm \hat{\mathbf{y}}\cos(\Delta\varphi_{\omega,2\omega})$, where $\hat{\mathbf{m}}$ is the current unit vector, and $\hat{\mathbf{x}}$ and $\hat{\mathbf{y}}$ are unit vectors pointing in the *x* and *y* directions, respectively (ref. [29]). Beams with opposite handedness do not produce an appreciable current[30].

Here we consider a modified arrangement where we begin with a radially polarized 2ω beam and demonstrate that a circularly polarized ω beam can be used to adjust the current pattern between radial and azimuthal configurations, that is $|i\rangle = c_r|r\rangle + c_a|a\rangle$. Because the field vector of the radial 2ω beam rotates through 2π as the azimuthal coordinate is traversed, OAM (topological charge, $m=1$) must be imparted to the circularly polarized ω beam so that its field vector rotates equally. This ensures that the relative field direction is matched at each azimuthal coordinate, producing azimuthally uniform coherent control.

Snapshots of the electric field evolution of the ω beam over half an optical cycle are shown in Fig. 5a–e, where it can be observed that the electric field rotates between radial and azimuthal configurations. Similarly, the oscillating radial 2ω electric field is depicted in Fig. 5f–j. The intensity distribution, polarization configuration and OAM of the ω and 2ω beams are summarized schematically in Fig. 5k,l, respectively. The 2ω beam can equivalently be represented as a superposition of left- and right-circularly polarized beams with opposite OAM, that is $m=\pm1$. In this view, photons matching the handedness of the ω beam contribute to the generated current, and those of opposite handedness do not.

The 2ω beam can also be thought of as one that carries information, and defines the relative amplitude and direction of currents at each pixel in the *xy* plane. The ω beam acts as a control beam that rotates the constructively interfering conduction-band population in the k_xk_y momentum plane by an angle $\Delta\varphi_{\omega,2\omega}$ (Fig. 5m), and therefore rotates the local current direction at each pixel by $\Delta\varphi_{\omega,2\omega}$ (Fig. 5n).

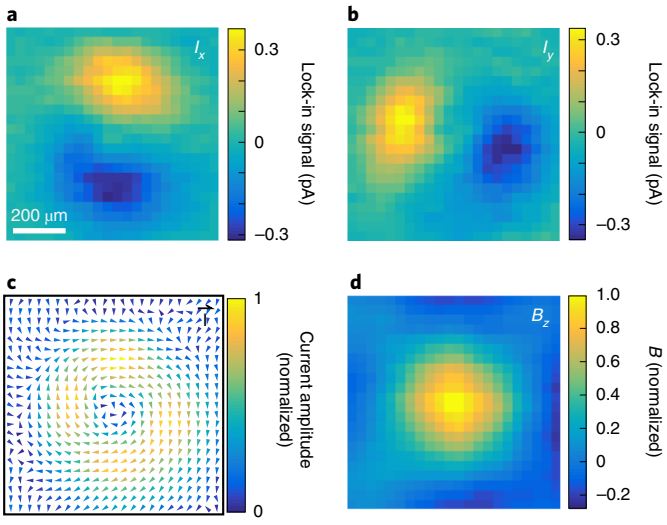

Fig. 3 | Measurement of azimuthal currents. a,**b**, Spatial scans of the detected *x* component (**a**) and *y* component (**b**) of the current injected via coherent control. **c**, A vector distribution of the photoexcited currents, demonstrating a ring-like current distribution. **d**, Calculated longitudinal magnetic field obtained by applying the Biot–Savart law to the measured data in **a** and **b**.

Using this scheme, we adjust $\Delta\varphi_{\omega,2\omega}$ in steps of 13.8° and perform a spatial current scan at each step. Here we measure only I_y and invoke symmetry to approximate I_x (Supplementary Notes 7 and 8). Figure 6a–d shows the current distribution for $\Delta\varphi_{\omega,2\omega}=-138°$, −69°, 41° and 124°, respectively. Decomposing each measurement into its $|r\rangle$ and $|a\rangle$ content, we plot c_r and c_a versus $\Delta\varphi_{\omega,2\omega}$ in Fig. 6e. As in the case where both beams had radial polarization,

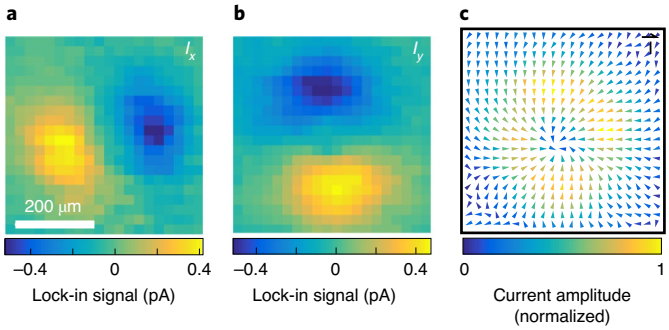

Fig. 4 | Measurement of radial currents. a,**b**, Spatial scan of the *x* component (**a**) and *y* component (**b**) of current excited by the synthesized $\omega/2\omega$ pulses. **c**, Current vector distribution, depicting a charge density wave towards the centre of the beam.

clear control over the radial content of the current is achieved. However, unlike the previous cases, we simultaneously control the azimuthal content of the current.

The radial component of each of these distributions is shown in Fig. 6f–i. Consistent with Fig. 6e, clear radial content is observed in Fig. 6f,h and absent in Fig. 6g,i. Rather than plotting the complementary azimuthal component, we instead plot the B_z distribution in Fig. 6j–m, which relates directly to the azimuthal current. In the same manner as with two azimuthal beams, adjusting $\Delta\varphi_{\omega,2\omega}$ changes the amplitude and direction of B_z (Supplementary Note 9).

We note the intriguing resemblance that these results bear to well-understood strong-field coherent control. In the quantum limit, we have emphasized that control arises from interference between one- and two-photon pathways to the same final state. As the energy separating the initial and final states of a system is increased, coherent control evolves from quantum interference into a strong field interaction.

To illustrate this connection, we consider tunnel ionization induced by intense $\omega/2\omega$ optical fields and the subsequent acceleration of photoelectrons to produce a photocurrent. Since tunnelling is sharply dependent on the field, the time window for creating a tunnelling wave packet is relatively precisely defined, that is, ionization is confined to brief bursts within the exciting electric field. In this regime, $\Delta\varphi_{\omega,2\omega}$ adjusts the temporal structure of the driving electric field and the time intervals over which tunnelling occurs. Electrons subsequently gain their velocity from the time-dependent force acting on them from their moment of birth until the optical waveform subsides. Their final momentum is proportional to the vector potential of the combined $\omega/2\omega$ laser field. When both beams have the same linear polarization, the vector potential acts along a single coordinate axis.

Making the strong ω beam circularly polarized, $\mathbf{E}_\omega(t) = E_{0,\omega}(\hat{\mathbf{x}}\cos(\omega t) + \hat{\mathbf{y}}\sin(\omega t))$, where t is time, provides two orthogonal field components oscillating 90° out of phase. Tunnelling

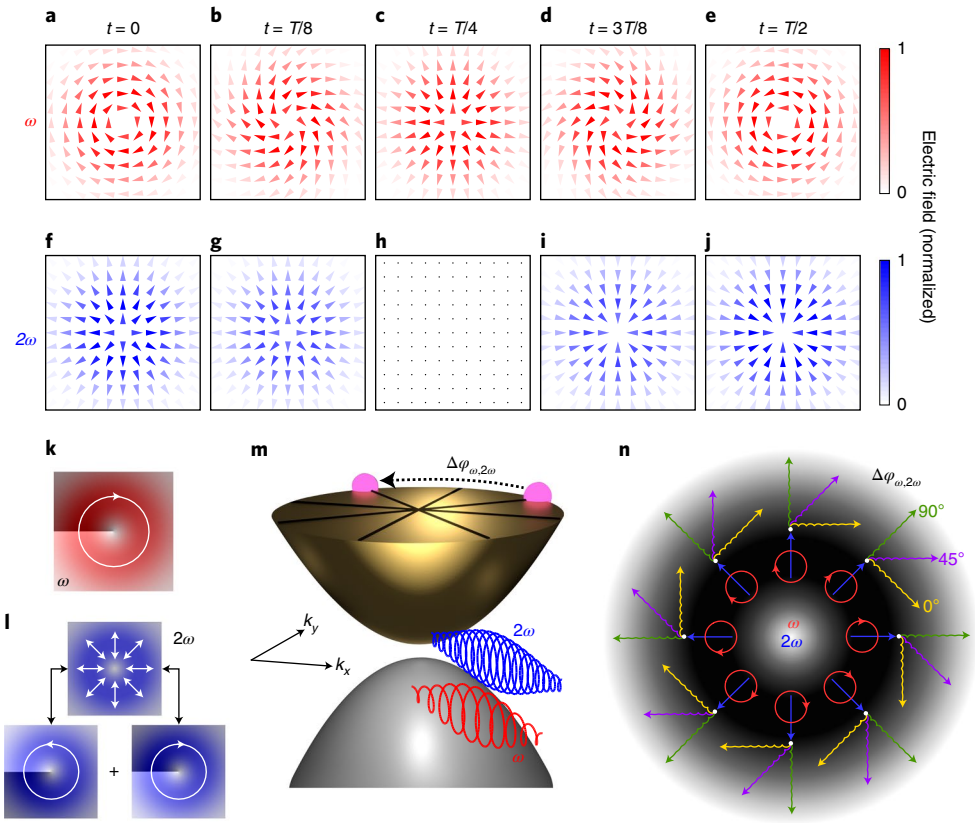

Fig. 5 | Two-dimensional control over the local current direction. a–**e**, Snapshots depicting the electric field rotation of a circularly polarized ω beam with $m=1$ over half an optical cycle, shown for $t=0$ (**a**), $t=T/8$ (**b**), $t=t/4$ (**c**), $t=3T/8$ (**d**), $t=T/2$ (**e**) (T is the optical period corresponding to ω; t is time). **f**–**j**, Temporal evolution of a radially polarized 2ω beam over half an optical cycle, with snapshots shown for $t=0$ (**f**), $t=T/8$ (**g**), $t=t/4$ (**h**), $t=3T/8$ (**i**), $t=T/2$ (**j**). **k**, Schematic summary of the ω beam, where the red colour map portrays the electric field amplitude, the circular arrow represents circular polarization and the grey scale conical gradient depicts $m=1$. **l**, Sketch of the 2ω beam properties. Notably, a radially polarized beam can be equivalently represented as a superposition of two circularly polarized beams with opposite handedness possessing $m=+1$ and $m=-1$. **m**, Illustration of coherent control in a semiconductor using two circularly polarized beams. Circular polarization enables control over the *x*- and *y*-momentum components by adjustment of $\Delta\varphi_{\omega,2\omega}$. **n**, Spatial arrangement of the controlled currents for $\Delta\varphi_{\omega,2\omega}=0°$ (yellow), 45° (purple) and 90° (green).

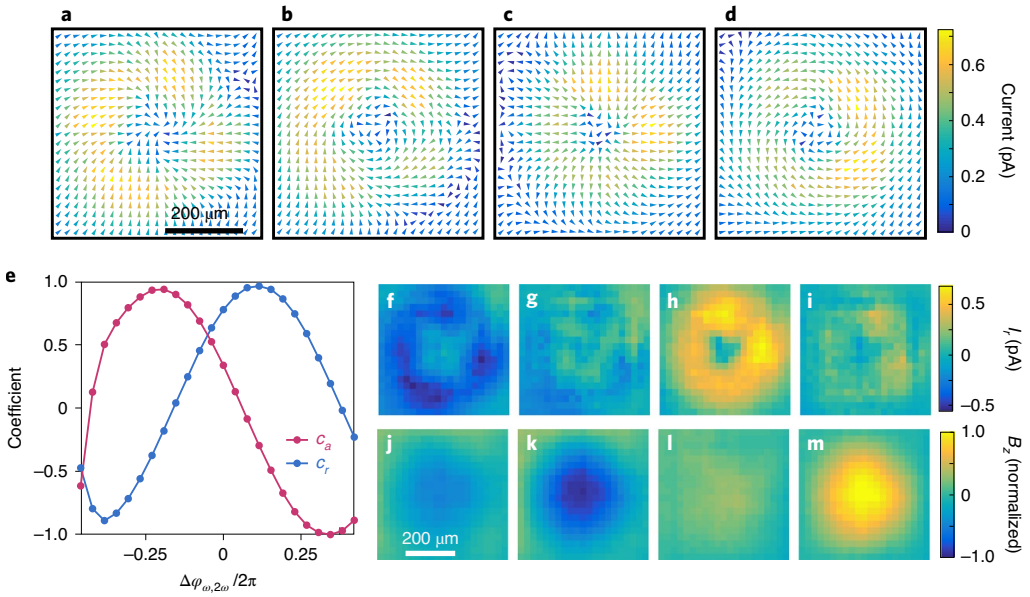

Fig. 6 | Coherent control of orthogonal current modes. a–d, The photoinjected current distribution as the relative phase delay between the circularly polarized beam (ω) and the radially polarized beam (2ω) for $\Delta\varphi_{\omega,2\omega} = -138°$ (**a**), −69° (**b**), 41° (**c**) and 124° (**d**). **e**, Coefficients c_a and c_r representing the relative radial and azimuthal content of the current mode as $\Delta\varphi_{\omega,2\omega}$ is scanned in 13.8° steps. In these distributions, only the *y* component of the current is measured and rotational symmetry is assumed to obtain the *x* component, as discussed in Supplementary Notes 7 and 8. **f–i**, The radial component of **a–d**, respectively. **j–m**, The longitudinal magnetic field, B_z, of **a–d**, respectively.

dynamics within the two-dimensional vector potential can be controlled using a weak, linearly polarized 2ω beam with adjustable polarization. The total electric field (and therefore the tunnelling rate) is maximized when the phase of the circularly polarized beam is such that its field direction passes the polarization direction of the linearly polarized 2ω beam at the field crest of the 2ω beam.

Strong-field physics requires that, once released from the atom, the electron's final drift is approximately confined to the plane of polarization (for non-relativistic beams) and in the direction perpendicular to the direction that the fundamental field was pointing when the electron tunnelled[42]. Adjustment of $\Delta\varphi_{\omega,2\omega}$ and the 2ω polarization orientation controls the ω polarization at the tunnelling instants, which determines the *x* and *y* components of the subsequent photocurrent.

By replacing the linearly polarized 2ω beam with a radially polarized beam, and adding $m = 1$ to the circularly polarized ω beam, we arrive at the strong-field analogue of the experiment presented in Figs. 5 and 6. In the same manner as we have demonstrated in LT-GaAs, $\Delta\varphi_{\omega,2\omega}$ can be used to control the local current direction, which transforms the global current distribution between radial and azimuthal patterns. While the concept is very different, the quantum and classical scenarios reach qualitatively similar outcomes.

Discussion

In summary, we have demonstrated a unique measurement technique that gives access to the complete vectorial arrangement of currents in a semiconductor. Using this, we have shown that coherent control can be exercised with any combination of ω and 2ω beams sharing the same vector mode, resulting in a current distribution resembling the vector mode. This indirectly demonstrates that the local current density excited in each $\sim\lambda^2$ area pixel of the semiconductor can be precisely adjusted to an amplitude[7] up to ~kA cm^{-2} and directed in any transverse direction. Near-field methods or metamaterials will allow this to be extended to a subwavelength scale. We envisage that simplified coherent control schemes and geometric electrode configurations optimized to detect a particular mode could make these principles useful in optical communications.

Furthermore, we have demonstrated a scheme for generating arbitrary superpositions of orthogonal current modes, demonstrating the potential for reconfigurable 'virtual' optoelectronic circuits. In particular, we note that this scheme involves two-photon transitions where each photon carries two quanta of angular momentum, and spin polarization of the resulting photocurrents remains a fascinating topic that has not yet been examined in detail. These results open numerous frontiers in coherent control, including dynamic manipulation of two-dimensional optoelectronic circuits, excitation of intense magnetic fields with femtosecond rise times and generation of magnetic lattices for magnetic materials, similar to optical lattices that have become so important.

Online content

Any methods, additional references, Nature Research reporting summaries, source data, extended data, supplementary information, acknowledgements, peer review information; details of author contributions and competing interests; and statements of data and code availability are available at https://doi.org/10.1038/s41566-020-0690-1.

Received: 3 March 2020; Accepted: 7 August 2020;
Published online: 14 September 2020

References

1. Shapiro, M. & Brumer, P. *Quantum Control of Molecular Processes* (John Wiley & Sons, 2012).
2. Garcia-Ripoll, J. J., Zoller, P. & Cirac, J. I. Speed optimized two-qubit gates with laser coherent control techniques for ion trap quantum computing. *Phys. Rev. Lett.* **91**, 157901 (2003).
3. Scharfenberger, B., Munro, W. J. & Nemoto, K. Coherent control of an NV$^-$ center with one adjacent ^{13}C. *New J. Phys.* **16**, 093043 (2014).
4. Wang, J. I.-J. et al. Coherent control of a hybrid superconducting circuit made with graphene-based van der Waals heterostructures. *Nat. Nanotechnol.* **14**, 120–125 (2019).
5. Corkum, P. B. & Krausz, F. Attosecond science. *Nat. Phys.* **3**, 381–387 (2007).

6. Boutu, W. et al. Coherent control of attosecond emission from aligned molecules. *Nat. Phys.* **4**, 545–549 (2008).
7. Haché, A., Sipe, J. E. & van Driel, H. M. Quantum interference control of electrical currents in GaAs. *IEEE J. Quantum Electron.* **34**, 1144–1154 (1998).
8. Viteau, M. et al. Optical pumping and vibrational cooling of molecules. *Science* **321**, 232–234 (2008).
9. Lien, C.-Y. et al. Broadband optical cooling of molecular rotors from room temperature to the ground state. *Nat. Commun.* **5**, 4783 (2014).
10. Dupont, E., Corkum, P. B., Liu, H. C., Buchanan, M. & Wasilewksi, Z. R. Phase-controlled currents in semiconductors. *Phys. Rev. Lett.* **74**, 3596–3599 (1995).
11. Stevens, M. J. et al. Optical injection and coherent control of a ballistic charge current in GaAs/AlGaAs quantum wells. *J. Appl. Phys.* **94**, 4999–5004 (2003).
12. Atanasov, R., Haché, A., Hughes, J. L. P., van Driel, H. M. & Sipe, J. E. Coherent control of photocurrent injection in bulk semiconductors. *Phys. Rev. Lett.* **76**, 1703–1706 (1996).
13. Fraser, J. M., Shkrebtii, A. I., Sipe, J. E. & van Driel, H. M. Quantum interference in electron–hole generation in noncentrosymmetric semiconductors. *Phys. Rev. Lett.* **83**, 4192–4195 (1999).
14. Côté, D., Fraser, J. M., DeCamp, M., Bucksbaum, P. H. & van Driel, H. M. THz emission from coherently controlled photocurrents in GaAs. *Appl. Phys. Lett.* **75**, 3959–3961 (1999).
15. Fraser, J. M. & van Driel, H. M. Quantum interference control of free-carrier density in GaAs. *Phys. Rev. B.* **68**, 085208 (2003).
16. Costa, L., Betz, M., Spasenovic, M., Bristow, A. D. & van Driel, H. M. All-optical injection of ballistic electrical currents in unbiased silicon. *Nat. Phys.* **3**, 632–635 (2007).
17. Spasenovic, M., Betz, M., Costa, L. & van Driel, H. M. All-optical coherent control of electrical currents in centrosymmetric semiconductors. *Phys. Rev. B* **77**, 085201 (2008).
18. Schiffrin, A. et al. Optical-field-induced currents in dielectrics. *Nature* **493**, 70–74 (2013).
19. Sederberg, S. et al. Attosecond optoelectronic field measurement in solids. *Nat. Commun.* **11**, 430 (2020).
20. Güdde, J., Rohleder, M., Meier, T., Koch, S. W. & Höfer, U. Time-resolved investigation of coherently controlled electric currents at a metal surface. *Science* **318**, 1287–1291 (2007).
21. Newson, R. W., Ménard, J. –M., Sames, C., Betz, M. & van Driel, H. M. Coherently controlled ballistic charge currents in single-walled carbon nanotubes and graphite. *Nano Lett.* **8**, 1586–1589 (2008).
22. Rybka, T. et al. Sub-cycle optical phase control of nanotunnelling in the single-electron regime. *Nat. Photon.* **10**, 667–670 (2016).
23. Higuchi, T., Heide, C., Ullmann, K., Weber, H. B. & Hommelhoff, P. Light-field-driven currents in graphene. *Nature* **550**, 224–228 (2017).
24. Pierce, D. T. & Meier, F. Photoemission of spin-polarized electrons from GaAs. *Phys. Rev. B* **13**, 5484–5500 (1976).
25. Pierce, D. T. et al. The GaAs spin polarized electron source. *Rev. Sci. Instrum.* **51**, 478–499 (1980).
26. Ivchenko, E. L. & Pikus, G. E. New photogalvanic effect in gyrotropic crystals. *JETP Lett.* **27**, 604–608 (1978).
27. Belinicher, V. I. Space-oscillating photocurrent in crystals without symmetry center. *Phys. Lett. A* **66**, 213–214 (1978).
28. Asnin, V. M. et al. Observation of a photo-emf that depends on the sign of the circular polarisation of the light. *JETP Lett.* **28**, 74–77 (1978).
29. Bhat, R. D. R. & Sipe, J. E. Optically injected spin currents in semiconductors. *Phys. Rev. Lett.* **85**, 5432–5435 (2000).
30. Stevens, M. J. et al. Coherent control of an optically injected ballistic spin-polarized current in bulk GaAs. *J. Appl. Phys.* **91**, 4382–4386 (2002).
31. Stevens, M. J. et al. Quantum interference control of ballistic pure spin currents in semiconductors. *Phys. Rev. Lett.* **90**, 136603 (2003).
32. Hübner, J. et al. Direct observation of optically injected spin-polarized currents in semiconductors. *Phys. Rev. Lett.* **90**, 216601 (2003).
33. Fickler, R. et al. Quantum entanglement of high angular momenta. *Science* **338**, 640–643 (2012).
34. Mair, A., Vaziri, A., Weihs, G. & Zeilinger, A. Entanglement of the orbital angular momentum states of photons. *Nature* **412**, 313–316 (2001).
35. Wang, J. et al. Terabit free-space data transmission employing orbital angular momentum multiplexing. *Nat. Photon.* **6**, 488–496 (2012).
36. Hell, S. W. & Wichmann, J. Breaking the diffraction resolution limit by stimulated-emission: stimulated-emission-depletion fluorescence microscopy. *Opt. Lett.* **19**, 780–782 (1994).
37. Padgett, M. & Bowman, R. Tweezers with a twist. *Nat. Photon.* **5**, 343–348 (2011).
38. Schmiegelow, C. T. et al. Transfer of optical orbital angular momentum to a bound electron. *Nat. Commun.* **7**, 12998 (2016).
39. Wätzel, J. & Berakdar, J. Centrifugal photovoltaic and photogalvanic effects driven by structured light. *Sci. Rep.* **6**, 21475 (2016).
40. Wätzel, J., Granados-Castro, C. M. & Berakdar, J. Magnetoelectric response of quantum structures driven by optical vector beams. *Phys. Rev. B* **99**, 085425 (2019).
41. Sederberg, S., Kong, F. & Corkum, P. B. Tesla-scale terahertz magnetic impulses. *Phys. Rev. X* **10**, 011063 (2020).
42. Corkum, P. B., Burnett, N. H. & Brunel, F. Above-threshold ionization in the long-wavelength limit. *Phys. Rev. Lett.* **62**, 1259–1262 (1989).

Methods

Optical system. A Coherent Legend laser amplifier (carrier wavelength, $\lambda = 800$ nm; repetition rate, $f_{rep} = 1$ kHz; pulse energy, $E_p = 5$ mJ; pulse duration, $\tau_p = 30$ fs) is used to pump an optical parametric amplifier (Light Conversion TOPAS). The signal output from the optical parametric amplifier ($\lambda = 1{,}482$ nm, $E_p = 400$ μJ, $\tau_p = 40$ fs) is passed through a half-wave plate and wiregrid polarizer to control the pulse energy. After passing the pulse through a beta-barium borate frequency doubling crystal, the $\omega/2\omega$ pulse pair is directed into an interferometer, where the two colours are separated using a dichroic mirror. Further details are available in Supplementary Note 10. The ω pulse is directed through a fixed optical path, while the relative timing of the 2ω pulse is controlled using a delay stage with a piezoelectric actuator. Following the last mirror before beam recombination, each pulse is passed through a wiregrid polarizer to obtain linear polarization and then through a liquid crystal plate to convert the Gaussian mode into the desired vector beam. After recombination using a dichroic mirror at near-normal incidence, the beams are focused to a spot diameter of approximately 300 μm using a biconvex lens with focal length, $f = 500$ mm. An iris is closed on the second harmonic beam to match its size to the fundamental beam in the detection plane. Although the two beams do not focus in exactly the same plane, the relatively loose focusing minimizes effects related to non-uniform relative phase across the beam profile.

Vector beam generation. Liquid crystal plates (q plates) with topological charge, $q = 1/2$, are used to convert beams with s polarization into azimuthal polarization, p polarization into radial polarization and circular polarization (obtained by inserting an additional quarter-wave plate) into circularly polarized vortex beams with $m = 1$. A radio-frequency voltage signal is applied to indium tin oxide electrodes on the q plate, where the amplitude of this signal tunes the operational wavelength of the q plate. Details on the fabrication of the q plates are available in Supplementary Note 12.

Detector fabrication. Two large aluminium electrodes separated by a 25 μm gap are deposited onto the detection substrate using a shadow mask and electron beam deposition. The substrate consists of a 1.2-μm-thick LT-GaAs film epitaxially grown onto GaAs. The sample is mounted to a printed circuit board and the electrodes are electrically contacted to it. An identical pair of electrodes is deposited onto a 150-μm-thick fused silica substrate. This substrate is used as an optical mask, and is mounted approximately 100 μm above the LT-GaAs detector, but with the electrodes oriented in the orthogonal direction. The two orthogonal pairs of electrodes form a 25 μm × 25 μm square aperture, which limits the exposure of the LT-GaAs detector to a 25 μm × 25 μm pixel of the beam.

Detection scheme. The LT-GaAs detector is connected to a lock-in amplifier (Stanford Research Systems SR830, further details in Supplementary Note 13). The reference frequency is obtained by amplitude modulating the 2ω optical path at 500 Hz using a mechanical chopper. The detector is raster scanned across the beam profile using two motorized stages. At each stage position, the lock-in signal is accumulated over 500 ms (250 laser shots) before the amplified current is read out. Each scan of the spatial mode takes approximately 15 min.

Data availability

The data that support the findings of this study are available from the corresponding author upon reasonable request.

Acknowledgements

This research was supported by the Natural Sciences and Engineering Research Council of Canada (NSERC) Discovery Grant Program, the Canada Research Chairs programme, the United States Defense Advanced Research Projects Agency ('Topological Excitations in Electronics (TEE)', agreement number D18AC00011) and the United States Army Research Office (award number W911NF-19-1-0211).

Author contributions

P.B.C. conceived the idea and supervised the project. S.S. and F.K. fabricated the detector and performed the experiments. S.S. conceived the measurement technique, analysed the data and wrote the manuscript. F.H. fabricated the q plates, supervised by E.K. All authors discussed the results and contributed to the manuscript.

Competing interests

The authors declare no competing interests.

Additional information

Supplementary information is available for this paper at https://doi.org/10.1038/s41566-020-0690-1.

Correspondence and requests for materials should be addressed to S.S.